Nano Research

Open Access

Research Article

In situ polymerization of poly(3,4-ethylenedioxythiophene) protective layer towards stable zinc anode

Debin Luo[1], Peng Zhou[1], Xiaowei Lv[1,2] ✉, Panpan Sun[1], Xiaohua Sun[1] ✉, and Hewei Zhao[3] ✉

[1] *College of Materials and Chemical Engineering, Key Laboratory of Inorganic Nonmetallic Crystalline and Energy Conversion Materials, China Three Gorges University, Yichang 443002, China*
[2] *Hubei Three Gorges Laboratory, Yichang 443007, China*
[3] *School of Chemistry, Beihang University, Beijing 100191, China*

Cite this article: *Nano Research*, **2025**, *18*, 94907037. https://doi.org/10.26599/NR.2025.94907037

ABSTRACT: Aqueous zinc-ion devices are considered promising candidates for energy storage due to their high safety, low cost and relatively high energy density. However, the dendrite growth, hydrogen evolution reaction (HER) and corrosion of the zinc anode significantly limit the development of Zn-ion devices. Here, an inexpensive poly(3,4-ethylenedioxythiophene) (PEDOT) protective layer was constructed *in situ* on the Zn surface using electro-polymerization to suppress dendrite growth and side reactions, thereby enhancing the reversibility of Zn. Experimental and theoretical calculations revealed that this hydrophilic protective layer promotes the desolvation process of hydrated Zn^{2+} and facilitates the transport of zinc ions, thus improving the thermodynamic and kinetic properties of Zn^{2+} deposition and inhibiting interfacial side reactions. Consequently, the optimized PEDOT@Zn symmetric battery exhibited a cycling stability exceeding 1250 h at 0.5 mA·cm^{-2} and 0.25 mAh·cm^{-2}, with a significantly reduced overpotential (from 91.8 to 35 mV). With the assistance of the PEDOT protective layer, the PEDOT@Zn//Cu battery maintained approximately 99.5% Coulombic efficiency after 450 cycles. *Ex-situ* scanning electron microscopy (SEM) and *in situ* optical microscopy characterizations further confirmed that the PEDOT protective layer can effectively suppress the growth of zinc dendrites. Additionally, the Zn-ion capacitors assembled by the PEDOT@Zn and activated carbon also demonstrated outstanding cycling stability.

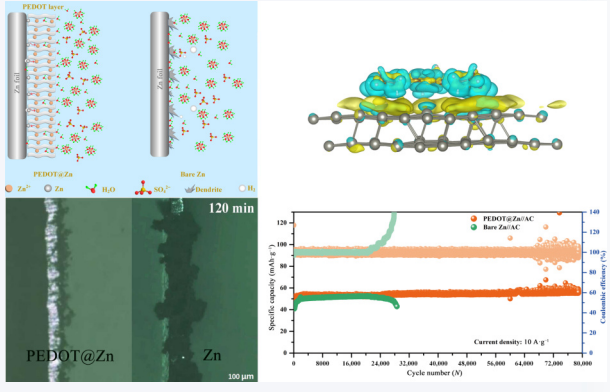

KEYWORDS: zinc-ion devices, zinc anode, poly(3,4-ethylenedioxythiophene) (PEDOT), dendrite, desolvation process

1 Introduction

With the growing demand for renewable energy sources, aqueous zinc-ion devices (aqueous zinc-ion batteries (ZIBs) and zinc-ion capacitors (ZICs)) including zinc metal anodes are considered one of the strongest candidates for next-generation energy storage devices due to their excellent electrochemical performance, intrinsic safety and low cost [1–3]. However, during battery operation, the interface between the Zn metal electrode and the aqueous electrolyte is prone to hydrogen evolution reaction (HER), along with the formation of non-conductive by-products and Zn dendrite growth. These non-conductive by-products can hinder electron transport and battery cycling on the zinc surface, while severe dendrite growth may penetrate the separator, leading to internal battery short-circuiting [4–7].

To address the aforementioned issues faced by the zinc anode, various strategies have been employed, including interface protective layer [5, 8], electrolyte additives [9–12], structural design [13–18] and alloying [17, 18]. Among them, constructing an artificial interface protective layer on the zinc anode is a simple and effective strategy with feasibility and practicability. For instance, the Cao research team utilized cyanoacrylate adhesive as a coating, which effectively reduced side reactions and inhibited dendrite growth, thus enhancing the cycling performance of full cells and symmetric cells. However, due to the coating's low conductivity, its introduction did not effectively reduce the overpotential [19]. In addition to good conductivity, the protective layer should also

Received: July 31, 2024; **Revised:** September 3, 2024
Accepted: September 15, 2024

✉Address correspondence to Xiaowei Lv, xwlv@ctgu.edu.cn; Xiaohua Sun, mksxh@163.com; Hewei Zhao, zhaohewei@buaa.edu.cn

possess excellent zinc ion transport capabilities. For example, He et al. employed Al_2O_3 as a zinc anode coating, separating the electrolyte from the zinc substrate, reducing side reactions, improving the uniformity of Zn plating/stripping and inhibiting the formation of Zn dendrites. This enhanced the capacity retention and rate performance of the full cell. Nevertheless, despite these achievements, the coating inevitably hindered the diffusion of zinc ions from the electrolyte to the zinc substrate, resulting in less significant improvements in the performance of symmetric cells [20]. Therefore, finding an ideal protective layer remains a significant challenge for zinc anodes.

In this work, we report a facile and cost-effective method of *in situ* growing poly(3,4-ethylenedioxythiophene) (PEDOT) as an interfacial protective layer on the zinc anode. The hydrophilic PEDOT protective layer, with its efficient zinc ion transport properties, reduces the two-dimensional (2D) diffusion of zinc ions, enabling uniform zinc deposition/stripping and minimizing dendrite growth. The PEDOT protective layer enhances the redox kinetics of zinc, significantly improving the stability of the metal anode. The symmetric cell exhibits excellent cycling stability over 1250 h at 0.5 mA·cm^{-2} and 0.25 mAh·cm^{-2} with a low overpotential of 35 mV. Furthermore, the Zn-ion capacitors assembled by the PEDOT@Zn and activated carbon (AC) demonstrate outstanding cycling performance with over 80,000 cycles at 10 A·g^{-1}.

2 Experimental

2.1 Experimental materials

Zinc foil (Zn, 99.9%); copper foil (Cu, 99.9%); zinc sulfate heptahydrate ($ZnSO_4{\cdot}7H_2O$, analytical reagent (AR)) were purchased from Aladdin Reagent Co., Ltd. Sodium dodecyl sulfate (SDS, AR), AC (AR), 3,4-ethylenedioxythiophene (EDOT, AR), N-methylpyrrolidone (NMP, AR), polyvinylidene fluoride (PVDF, 99.5%) and hydrochloric acid (HCl, 99.5%) were purchased from Macklin Biochemical Technology Co., Ltd. Potassium perchlorate ($KClO_4$, AR) was purchased from Chengdu Kelong Chemical Co., Ltd. All reagents were used without further purification.

2.2 *In situ* electropolymerization of poly(3,4-ethylenedioxythiophene) protective layer on zinc surface

PEDOT protective layers were deposited on zinc foil surfaces via *in situ* electropolymerization technology. Initially, 5.407 g of SDS and 1.558 g of potassium perchlorate ($KClO_4$) were uniformly dispersed in 120 mL of deionized water. Subsequently, 0.380 mL of EDOT was added dropwise to the above solution under stirring for 30 min. Then, PEDOT was deposited onto the zinc foil surface at a constant voltage of 1.2 V using a chronoamperometric technique. Zinc foil, cut into 2.5 × 2.5 cm squares and tape one side of them. Remove the tape when the polymerization is complete. Treated zinc foil served as the working electrode, while a platinum electrode was used as the counter electrode and an Ag/AgCl electrode served as the reference electrode. The PEDOT-coated zinc foil was dried at 60 °C for 4 h before use. The thickness of the PEDOT protective layer was controlled by varying the deposition time and designated as PEDOT*m*@Zn, where *m* = 100, 150, 250, 350 and 450 s.

2.3 Preparation of AC cathode

The cathode material was prepared following a method described in a previous study [21]. AC, conductive carbon black and polyvinylidene fluoride were mixed in N-methyl-2-pyrrolidone to form a slurry, which was then coated onto stainless steel foil. The coated foil was dried at 80 °C for 12 h before use. All electrode sheets were cut into 12 mm diameter disks for testing. The mass loading of AC on each electrode sheet was 0.8–1.2 mg·cm^{-2}.

2.4 Testing and characterization conditions

CR2032-type coin cells were assembled using 2 M $ZnSO_4$ as the electrolyte and a glass fiber separator (Whatman, GF/A) as the separator. Symmetric cells were assembled using two identical bare zinc or PEDOT-coated zinc foils and tested using a LAND multichannel battery tester. Half-cells using Zn//Cu or PEDOTm@Zn//Cu configurations were subjected to cycling tests and cyclic voltammetry (CV) measurements, with a scan rate of 1 mV·s^{-1} and a voltage window of −0.4 to 1.0 V. Tafel polarization curves, electrochemical impedance spectroscopy (EIS) and linear sweep voltammetry (LSV) were performed using a CHI760E electrochemical workstation, with a scan rate of 5 mV·s^{-1} and the frequency ranging of electrochemical impedance spectroscopy is 10^{-2}–10^5 Hz. The Zn-ion capacitors were assembled using bare zinc or PEDOT@Zn as anode and activated carbon as cathode using AC cathode and subjected to cycling tests using the LAND multichannel battery tester. Cyclic voltammetry and EIS of the full cells were conducted on the CHI760E electrochemical workstation, with a scan rate of 10 mV·s^{-1} and testing frequencies ranging from 10^{-2} to 10^5 Hz.

X-ray diffraction (XRD) patterns were obtained using a SmartLab X-ray diffractometer with Cu Kα (α = 1.5406 Å) as the radiation source. X-ray photoelectron spectroscopy (XPS) was performed using a Kratos Analytical Axis Ultra DLD UHV spectrometer with an Al Kα X-ray source (1486.6 eV). Scanning electron microscopy (SEM) images were acquired using a JSM-7500F instrument to observe the surface morphology of the zinc electrodes and coated electrodes. Fourier transform infrared spectroscopy (FTIR) measurements were performed using a Frontier NIR instrument in the range of 500 to 4000 cm^{-1} to detect the organic coatings on the surfaces.

2.5 Density functional theory (DFT) calculation

Vienna *ab-initio* simulation package (VASP) was used as the foundation for all DFT computations [22, 23]. The Perdew–Burke–Ernzerhof (PBE) functional in the generalized gradient approximation (GGA) approach explained the exchange-correlation effects [24, 25]. The projected augmented wave (PAW) approach was used to account for the core-valence interactions [26]. For plane wave expansions, 400 eV was chosen as the energy cutoff. With energy and force respectively, the structural optimization was finished. The 1 × 1 × 1 *K*-point was used to sample the Brillouin zone. The dispersion interactions were described using Grimme's DFT-D3 methodology.

The adsorption energies (E_{ads}) of Zn and H_2O are calculated by

$$E_{ads} = E_{*Zn} - E_{Zn} - E_{Sub} \quad (1)$$

$$E_{ads} = E_{*H_2O} - E_{H_2O} - E_{Sub} \quad (2)$$

where E_{Zn} and E_{*Zn} represent the energies before and after the adsorption of Zn on the substrates, respectively. E_{H_2O} and E_{*H_2O} represent the energies before and after the adsorption of H_2O on

the substrates. E_{Sub} is the energy of Zn-002 and Zn-PEDOT surfaces.

Finite element analysis (FEA). In this experiment, the COMSOL Multiphysics 6.2 software was used to simulate the electric field distribution at the interface between the anode and the electrolyte. In the whole model, the length of the two electrodes is set to 100 μm, the distance between the electrodes is 120 μm and a total of 6 protrusions on the substrate of the zinc anode are evenly distributed on the surface, the diameter and height of the protrusions are 5 μm and each protrusion is 5 μm apart. Among them, the electrolyte between the filled cathode and the anode is 2 M $ZnSO_4$ and its conductivity is 5 $S{\cdot}m^{-1}$, while the conductivity of the zinc anode is $1.5*10^6$ $S{\cdot}m^{-1}$, the conductivity of the coating is 0.02 $S{\cdot}m^{-1}$, the current density applied between the electrodes is 0.5 $mA{\cdot}cm^{-2}$ and the voltage is 0.5 V.

3 Results and discussion

First, a PEDOT protective layer was uniformly deposited onto the surface of the zinc electrode through *in situ* electropolymerization [27]. After cleaning and drying, the PEDOT@Zn sample was obtained, as depicted in Fig. 1(a). We studied the effect of coating thickness on the zinc anode by adjusting the electropolymerization time (Fig. S1 in the Electronic Supplementary Material (ESM)). Symmetric cells assembled with bare zinc and PEDOT@Zn of different thicknesses were tested for their cycling performance (Fig. S2 in the ESM). The test results indicated that the sample with a polymerization duration of 150 s exhibited the best cycling capability. Unless otherwise specified, all subsequent tests were conducted on samples with a polymerization duration of 150 s. The optical image of bare Zn (the inset of Fig. 1(b)) displays a well-defined metallic luster, while the SEM image (Fig. 1(b)) reveals

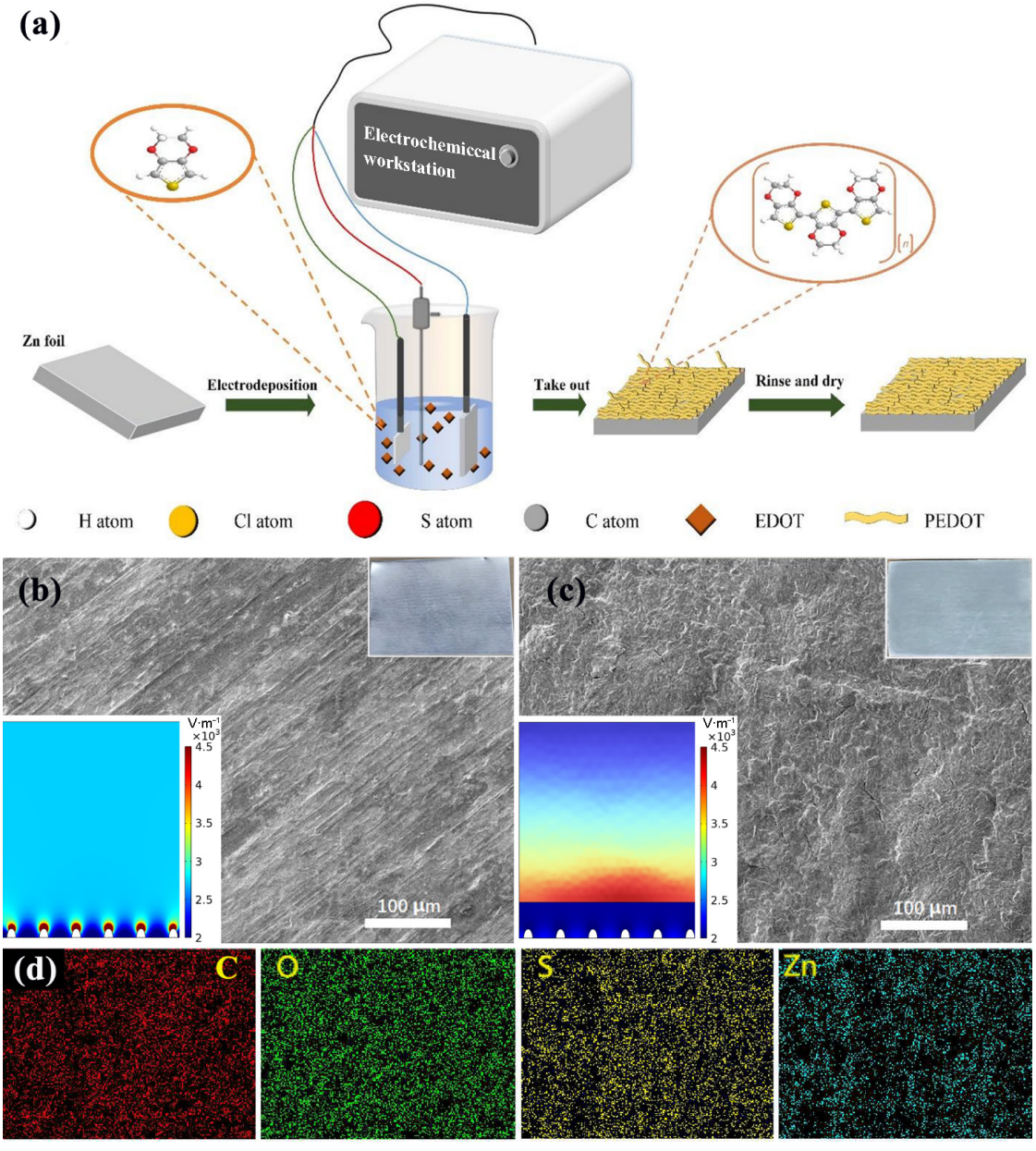

Figure 1 (a) Schematic diagram of *in situ* electropolymerization of PEDOT protective layer on zinc foil; optical image and numerical simulations of the electrical field distribution (inset) and SEM images of (b) pure Zn and (c) PEDOT@Zn; (d) EDS elemental mapping of the PEDOT@Zn.

significant unevenness on the Zn surface, which can lead to uneven electric field distribution and promote zinc dendrite formation. In contrast, the optical image of the PEDOT@Zn sample (the inset of Fig. 1(c)) shows a uniform semi-transparent coating adhering to the zinc surface. As illustrated in the inset of Fig. 1(b), an obvious uneven localized electric field on the Zn foil could be detected and the electric field intensity for these tip protuberances is sharply enhanced. Generally, such an uneven local electric field will trigger the Zn^{2+} ions to give priority to aggerate and deposit these protuberances, eventually evolving into dendrites. Inversely, the electric field on the PEDOT@Zn (the inset of Fig. 1(c)) is uniformly distributed which is conducive to eliminating the tip effect and promoting the uniform deposition of Zn^{2+} ions. The SEM image displays a layered structure of PEDOT covering the Zn surface (Fig. 1(c)). This indicates that zinc ions can diffuse from the electrolyte to the zinc substrate through these interspaces, without affecting the deposition and stripping of zinc ions. The energy dispersive spectroscopy (EDS) elemental mapping results demonstrate the presence of C, O, S and Zn elements on the sample surface, initially suggesting the successful preparation and uniform distribution of PEDOT on the zinc electrode surface, as shown in Fig. 1(d).

The X-ray diffraction data for both Zn and PEDOT@Zn samples in Fig. S3 in the ESM correspond to the standard card of pure zinc (PDF#65-5973), indicating that the PEDOT protective layer may exist in an amorphous form. To further demonstrate the successful preparation of the PEDOT protective layer on the Zn surface, XPS analysis was performed on PEDOT@Zn (Fig. S4 in the ESM). The high-resolution XPS spectrum of C 1s (Fig. 2(a)) revealed characteristic peaks at 284.6, 286 and 289.2 eV, corresponding to C–C/C=C, C–S and C–O bonds, respectively, consistent with previously reported C 1s peaks of PEDOT, further confirming the presence of PEDOT on zinc surface [28]. Additionally, FTIR of the PEDOT@Zn surface provided stronger evidence for the successful polymerization of PEDOT on the zinc surface (Fig. 2(b)). Specifically, the absorption peaks at 2920 and 2850 cm^{-1} were attributed to the stretching vibrations of C–H and CH_2 in the PEDOT structure. The peak at approximately 1630 cm^{-1} was due to the stretching vibration of C=C bonds. The peak at 1466 cm^{-1} was attributed to the stretching vibration of C–C bonds and the peaks at 1200 and 1058 cm^{-1} corresponded to the stretching vibrations of C–O and C–S bonds [29]. These atoms with high electronegativity are excellent zincophilic sites that attract zinc ions, facilitating the uniform distribution and accelerated transport of zinc ions on the zinc anode surface, promoting the uniform deposition/stripping of zinc ions. The remaining peaks represent absorption peaks of bending vibrations in the fingerprint region, further confirming the successful polymerization of the PEDOT coating on the zinc surface (Fig. 2(b)) [29, 30].

Symmetric battery testing is an effective approach to evaluate the electrochemical performance and durability of materials. Firstly, we tested the cycle life of symmetric batteries under different current densities and the results indicated a significant improvement in the cyclic performance of PEDOT@Zn compared to pure zinc symmetric batteries. As shown in Fig. 3(a), the PEDOT@Zn symmetric battery demonstrated a cycling duration of approximately 1250 h under 0.5 $mA·cm^{-2}$ and 0.25 $mAh·cm^{-2}$, approximately three times longer than that of the bare Zn symmetric battery (approximately 420 h). Even under the high current densities of 5 $mA·cm^{-2}$ and 2.5 $mAh·cm^{-2}$, the PEDOT@Zn symmetric battery still exceeded 240 h (Fig. 3(b)), approximately three times longer than the bare Zn symmetric battery (approximately 75 h). It is even better than most reported values for Zn symmetric battery (Table S1 in the ESM). The depth of discharge of the symmetric battery is 4.27%. Meanwhile, the overpotential of the PEDOT@Zn symmetric battery sample was only 35 mV at 0.5 $mA·cm^{-2}$ and even at 5 $mA·cm^{-2}$, the overpotential remained at 44.3 mV, significantly lower than the corresponding overpotentials of bare Zn (91.8 and 77.8 mV), indicating that the presence of the PEDOT protective layer enhanced the stability and reversibility of the zinc anode and during the plating/stripping process in the symmetric cell, faster ion transfer at the anode–electrolyte interface is responsible for the smaller concentration polarization, which is represented by the smaller voltage hysteresis [31, 32]. Additionally, to investigate the deposition kinetics of the zinc electrode, the symmetric batteries were cycled at different current densities (0.5 $mA·cm^{-2}$ to 5 $mA·cm^{-2}$). The exchange current density was calculated using the following equation [33, 34]

$$j = j_0 \times \frac{ZF\eta}{RT} \tag{3}$$

where j is the current density, η is the total overpotential, j_0 is the exchange current density, R and F represent the gas constant and Faraday constant, T is the thermodynamic temperature and Z is the number of electrons involved in the electrode reaction. As shown in Fig. 3(c), the fitted exchange current densities of bare Zn and PEDOT@Zn were obtained, indicating that the modified electrode exhibited a larger exchange current density (14.93 $mA·cm^{-2}$ > 8.13 $mA·cm^{-2}$), reflecting a smaller polarization effect under different current densities and greater zinc redox kinetics [35].

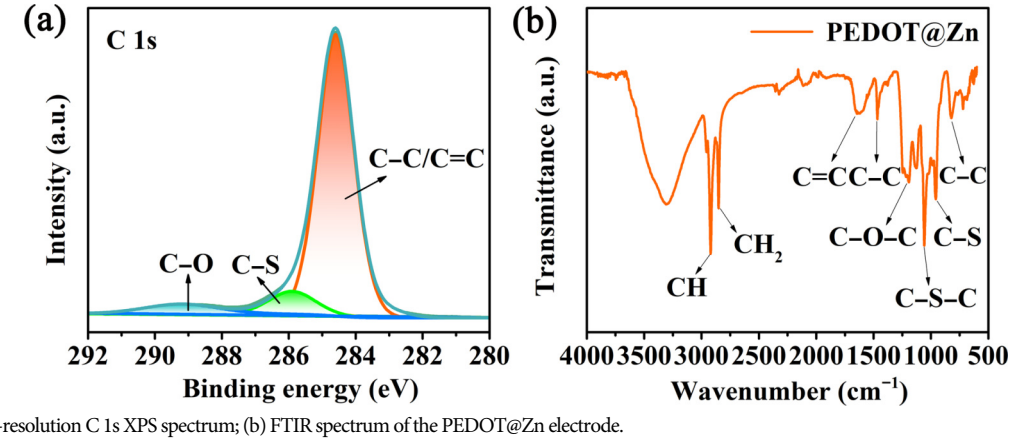

Figure 2 (a) High-resolution C 1s XPS spectrum; (b) FTIR spectrum of the PEDOT@Zn electrode.

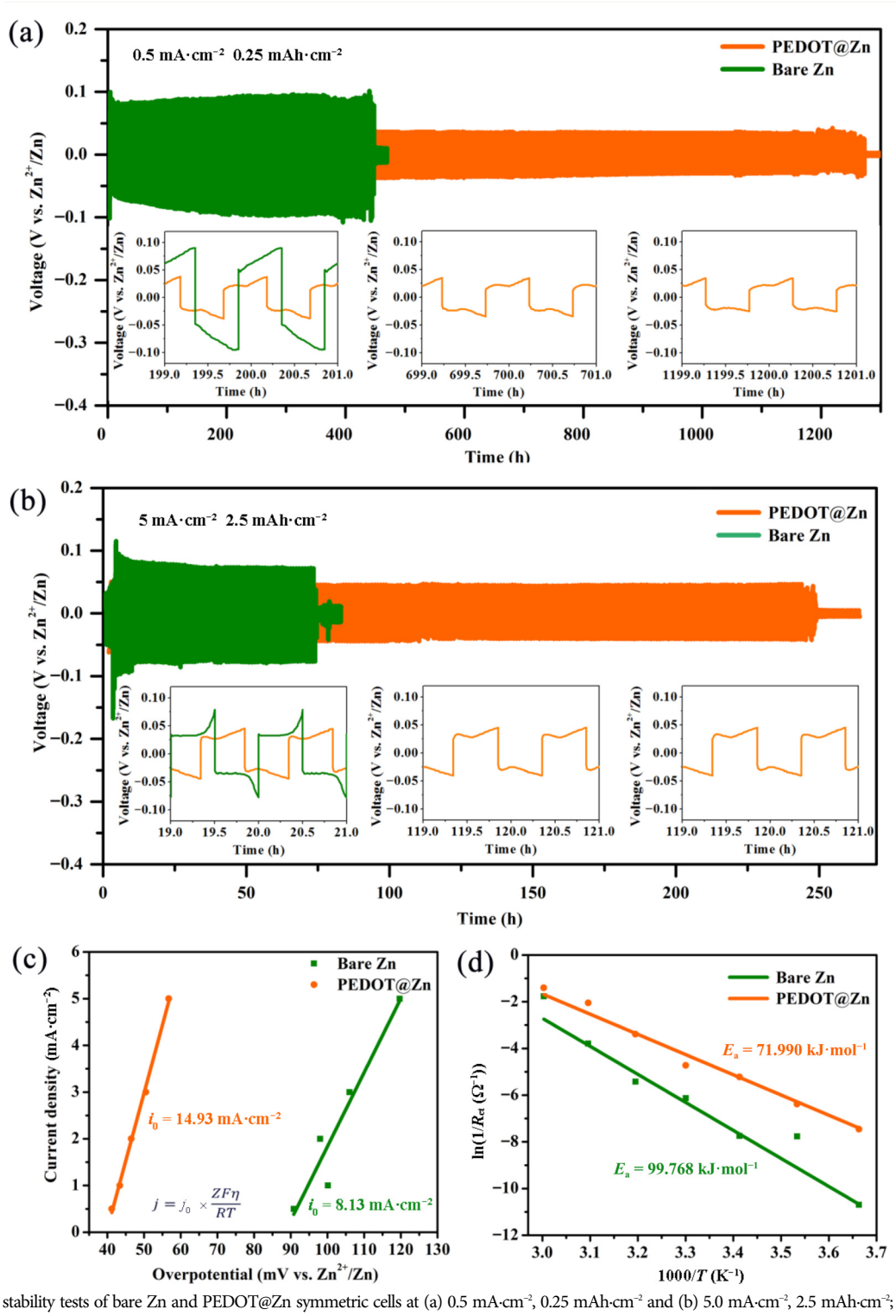

Figure 3 Cyclic stability tests of bare Zn and PEDOT@Zn symmetric cells at (a) 0.5 mA·cm^{-2}, 0.25 mAh·cm^{-2} and (b) 5.0 mA·cm^{-2}, 2.5 mAh·cm^{-2}; (c) exchange current densities of and (d) electron transfer activation energy plots for bare Zn and PEDOT@Zn.

Studies have revealed that in zinc salt aqueous solutions, zinc ions typically exist in the form of hydrated zinc ion clusters [36, 37]. During electrodeposition, hydrated zinc ions require a larger desolvation energy barrier compared to bare zinc ions to sustain the reduction reaction and yield zinc metal [38, 39]. To further investigate the transfer and desolvation processes of hydrated zinc ions, EIS tests were conducted on symmetric batteries assembled with bare Zn and PEDOT@Zn at various temperatures (Fig. S5 in the ESM). The test results were then fitted using an equivalent circuit diagram (Fig. S6 in the ESM) to obtain the resistance values of R_s (R_s is the fitting electrolyte resistance after the chronoamperometric test) and R_{ct} (R_{ct} is the fitting electronic transfer resistance after the chronoamperometric test) at different temperatures (Table S2 in the ESM). Experimental data showed

that the electron transfer resistance of bare zinc was greater than that of PEDOT@Zn across different temperatures (Fig. S6 and Table S1 in the ESM). Subsequently, the activation energy for electron transfer was calculated using the Arrhenius equation (Fig. 3(d)), which is given as follows [33, 39]

$$K = A\exp\left(-\frac{E_a}{RT}\right) \quad (4)$$

where R is the gas constant of 8.314 J·K^{-1}·mol^{-1}, K is the reaction rate constant, A is pre-exponential factor, E_a is activation energy, and T is the temperature of reactants in K. The fitted activation energy for electron transfer of bare Zn and PEDOT@Zn are 99.768 and 71.990 kJ·mol^{-1}, respectively, which demonstrated that the PEDOT layer can stimulate the Zn^{2+} desolvation step and facilitate ion migration kinetics. This may be attributed to the strongly electronegative S and O atoms in the protective layer, which facilitate the desolvation of hydrated zinc ions. This results in a reduced desolvation energy for zinc ions, thereby decreasing the energy consumption for the reduction reaction of zinc ions to produce zinc atoms.

To further validate the zinc deposition/stripping kinetics, Zn//Cu and PEDOT@Zn//Cu half-cells were assembled and subjected to cyclic voltammetry tests in the voltage range of −0.4 to 1.0 V (vs. Zn/Zn^{2+}), as shown in Fig. 4(a). The bare Zn and PEDOT@Zn curves exhibited similar shapes, indicating that the same electrochemical reactions involved in the zinc stripping/deposition process on Zn and PEDOT@Zn electrodes. Compared to the bare Zn electrode, the PEDOT@Zn anode showed larger oxidation and reduction currents, suggesting stronger reaction kinetics for the modified electrode. Nucleation overpotential tests at different current densities revealed that the PEDOT@Zn electrode exhibited lower nucleation overpotentials across various current densities (0.5, 1, 2, 4 mA·cm^{-2}) (Fig. S7 in the ESM and Fig. 4(b)), indicating

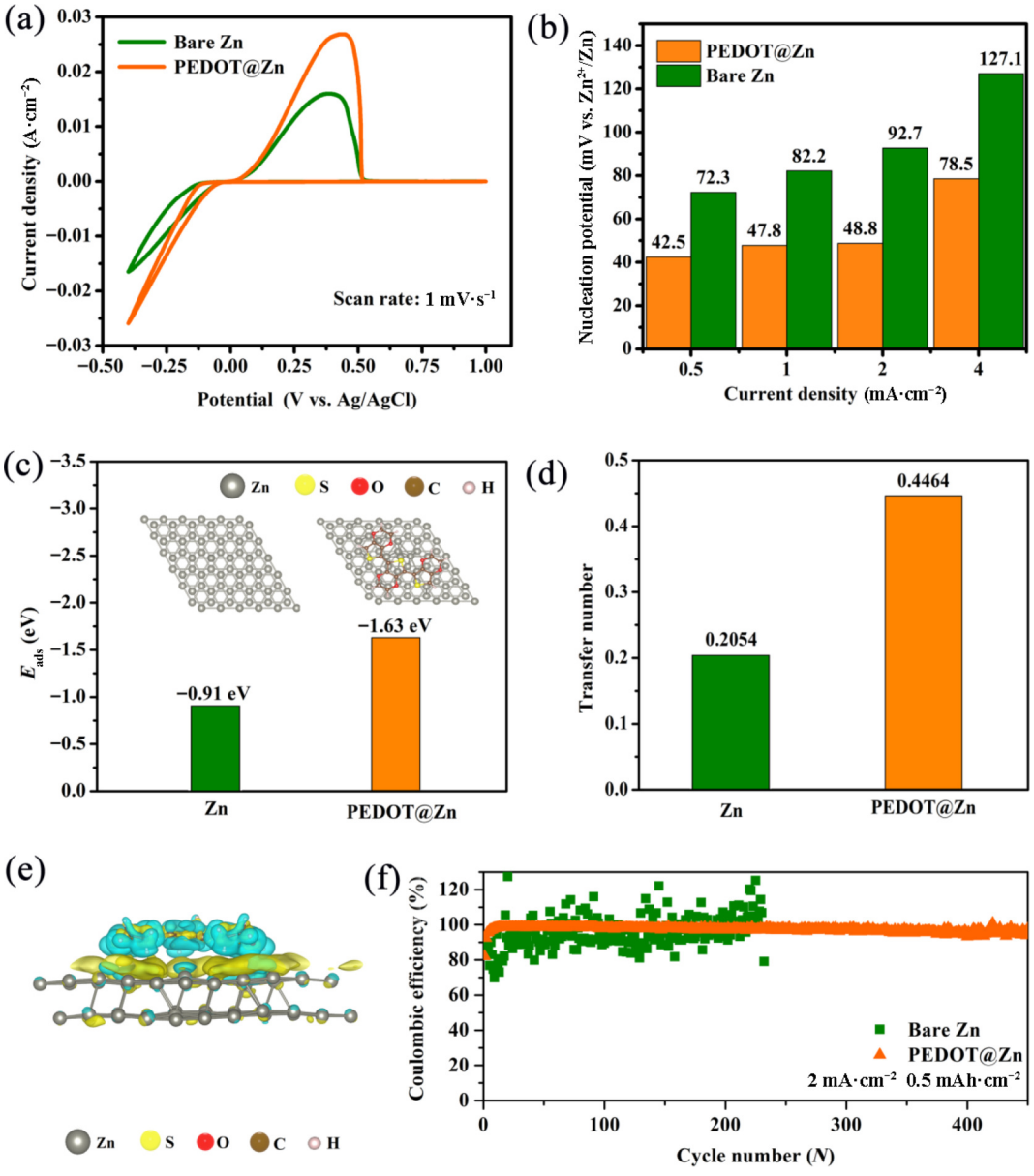

Figure 4 (a) Cyclic voltammetry scans of Zn//Cu and PEDOT@Zn//Cu half-cells; (b) nucleation overpotential comparison of Zn and PEDOT@Zn at 2 mA·cm^{-2}; (c) adsorption energy of zinc atoms on bare Zn and PEDOT@Zn; (d) comparison of Zn^{2+} transfer number of bare Zn and PEDOT@Zn. (e) Electron density difference map of PEDOT adsorbed on Zn surface; (f) Coulombic efficiency plot of bare Zn and PEDOT@Zn half-cell.

a lower potential barrier for zinc plating/stripping due to the presence of the PEDOT protective layer. To elucidate the reason for the improved deposition kinetics of the PEDOT@Zn electrode, the adsorption energy of zinc atoms on the surfaces of pure Zn and PEDOT@Zn plates was calculated based on DFT, as shown in Fig. 4(c). The results showed that the adsorption energy (E_{ads}) of Zn atoms on the pure Zn surface was −0.91 eV, while the adsorption energy on the PEDOT@Zn surface significantly increased to −1.63 eV, indicating better zinc ion transport and uniform deposition behavior of zinc atoms on the PEDOT@Zn surface [40–42]. To further understand zinc ion transport, transfer number tests were performed on Zn and PEDOT@Zn electrodes, as shown in Fig. S8 in the ESM and Fig. 4(d). The transfer number ($t_{Zn^{2+}}$) was calculated using the following equation [43, 44]

$$t_{Zn^{2+}} = \frac{I_S(\Delta V - I_0 R_0)}{I_0(\Delta V - I_s R_s')} \quad (5)$$

where ΔV represents the applied voltage (10 mV) during the chronoamperometric test. Here, R_0 and R_s' is electronic transfer resistances before and after the chronoamperometric test; I_0 and I_s are the initial and steady-state currents during the chronoamperometric test. The results indicate that the zinc ion transfer number for the PEDOT@Zn-assembled symmetric cell is 0.4464, which is significantly higher than that of bare Zn (0.2045). It may be affected by some zincophilic groups O and S in the PEDOT coating, which has an adsorption effect on zinc ions, which also accelerates the migration of zinc ions [45]. This increase in zinc ion transfer number allows timely replenishment of zinc ions consumed near the zinc substrate, alleviating the concentration gradient of zinc ions and reducing polarization effects caused by zinc ion concentration differences. The PEDOT protective layer also enhances the conductivity of zinc ions, thereby reducing the overpotential for zinc ion deposition/stripping [46]. Additionally, in the electron density difference map of PEDOT adsorbed on the Zn surface (Fig. 4(e)), where yellow represents charge accumulation regions and cyan represents charge deficiency regions, there is electron cloud overlap between Zn atoms and PEDOT, suggesting the existence of electron transfer between PEDOT and Zn metal, which favors uniform zinc deposition and stripping [47]. To further investigate the deposition and stripping behavior of PEDOT@Zn, Zn//Cu and PEDOT@Zn//Cu half-cells were assembled and subjected to charge–discharge cycling at 2 mA·cm^{-2} and 0.5 mAh·cm^{-2}, as shown in Fig. 4(f). The modified electrode exhibited more stable cycling performance and higher Coulombic efficiency compared to the bare Zn electrode. Specifically, the Coulombic efficiency of the modified electrode remained stable at around 99.5% after 450 cycles, indicating thorough zinc deposition and subsequent stripping, which significantly demonstrates the excellent reversibility and stability of the PEDOT@Zn electrode. The voltage–capacity curves (Fig. S9 in the ESM) of the half-cells show that the voltage hysteresis of the PEDOT@Zn//Cu half-cell is 64.8 mV, while the voltage hysteresis of the Zn//Cu half-cell is 73.1 mV. The modified electrode exhibits a lower voltage hysteresis, suggesting superior Zn^{2+} stripping/deposition capabilities and a lower nucleation energy barrier. When the capacity is increased to 1 mAh·cm^{-2}, as shown in Figs. S10 and S11 in the ESM, PEDOT@Zn//Cu half battery can still cycle stably 245 cycles and the Coulombic efficiency is also stable at 100%. By contrast, the Zn//Cu half battery began to fluctuate after the 92nd cycle and failed after 125 cycles. These data show that PEDOT@Zn half batteries exhibit better cycle performance at different capacities than pure zinc. This finding is consistent with the results of the zinc ion migration ability and low electronic transfer impedance tests [48].

Due to the contact between the zinc electrode and the electrolyte, a certain degree of corrosion and side reactions can occur. To investigate the corrosion resistance of bare Zn and PEDOT@Zn electrodes, Tafel polarization tests were conducted using a three-electrode system, with platinum as the counter electrode, zinc or modified zinc as the working electrode, Ag/AgCl as the reference electrode and 2 M $ZnSO_4$ as the electrolyte. The results indicated that the corrosion current density (j_{corr}) of the modified zinc electrode (1.66 mA·cm^{-2}) was significantly lower than that of the pure bare Zn electrode (2.34 mA·cm^{-2}), while the corrosion potential increased from −0.978 to −0.962 V (vs. Ag/AgCl) (Fig. 5(a)), demonstrating that the PEDOT coating exerts inhibitory effects on hydrogen evolution corrosion of zinc metal in both kinetic and thermodynamic aspects [49]. After immersing the bare zinc and PEDOT@Zn electrodes in 2 M $ZnSO_4$ for 7 days, XRD testing was performed (Fig. 5(b)). When the pure zinc electrode was immersed in the electrolyte for a week, characteristic peaks of the by-product $Zn_4SO_4(OH)_6{\cdot}xH_2O$ appeared on its surface, whereas no such by-product was observed on the surface of the PEDOT@Zn electrode, confirming the inhibitory effect of the PEDOT coating on by-product formation. The root cause is the formation of the following by-products, which occur in the following reactions [50, 51]

$$3Zn + 11H_2O + ZnSO_4 \rightarrow Zn_4(OH)_6SO_4 \cdot 5H_2O + H_2\uparrow \quad (6)$$

For pure zinc, Zn is in close contact with H_2O and $ZnSO_4$ in the electrolyte, so there will inevitably be a by-product $Zn_4SO_4(OH)_6{\cdot}5H_2O$. In the modified zinc anode, there is a PEDOT protective layer blocking between zinc metal and electrolyte, which reduces the possibility of contact between water and sulfuric acid electrolyte and zinc metal. Moreover, the layer has a desolvation effect to further avoid the contact between zinc metal and water, so that the coated zinc anode can inhibit the formation of by-products.

To investigate the hydrogen evolution side reaction on Zn and PEDOT@Zn electrodes, linear sweep voltammetry tests were conducted with a scan rate of 5 mV·s^{-1}, using Zn and PEDOT@Zn as working electrodes, platinum as the counter electrode and Ag/AgCl as the reference electrode (Fig. 5(c)). At a voltage of −1.5 V, the current density of PEDOT@Zn was 95.7 mA·cm^{-2}, significantly lower than the 118 mA·cm^{-2} of bare Zn, indicating a reduced tendency for hydrogen evolution side reactions [52]. The PEDOT protective layers may effectively isolate the active water and dissolved oxygen in the electrolyte from the zinc substrate, which is conducive to reducing hydrogen evolution side reactions, decreasing the possibility of cycling short-circuits due to zinc battery bulging and lowering the competing conjugate side reactions that interfere with the normal charge–discharge of zinc ions, thereby improving zinc utilization [53–55]. To further explore the effect of the PEDOT protective layer on inhibiting electrode corrosion, the contact angles of 2 M $ZnSO_4$ solution on zinc and PEDOT@Zn surfaces were measured (Fig. S12 in the ESM). The results show that the contact angle of PEDOT@Zn (26.96°) is lower than that of bare Zn (77.92°), indicating better hydrophilicity of the PEDOT protective layer. This may be attributed to the gaps in the PEDOT coating and some hydrophilic groups it contains, which promote the diffusion of the electrolyte, facilitating rapid diffusion of zinc ions on the electrode and reducing polarization caused by

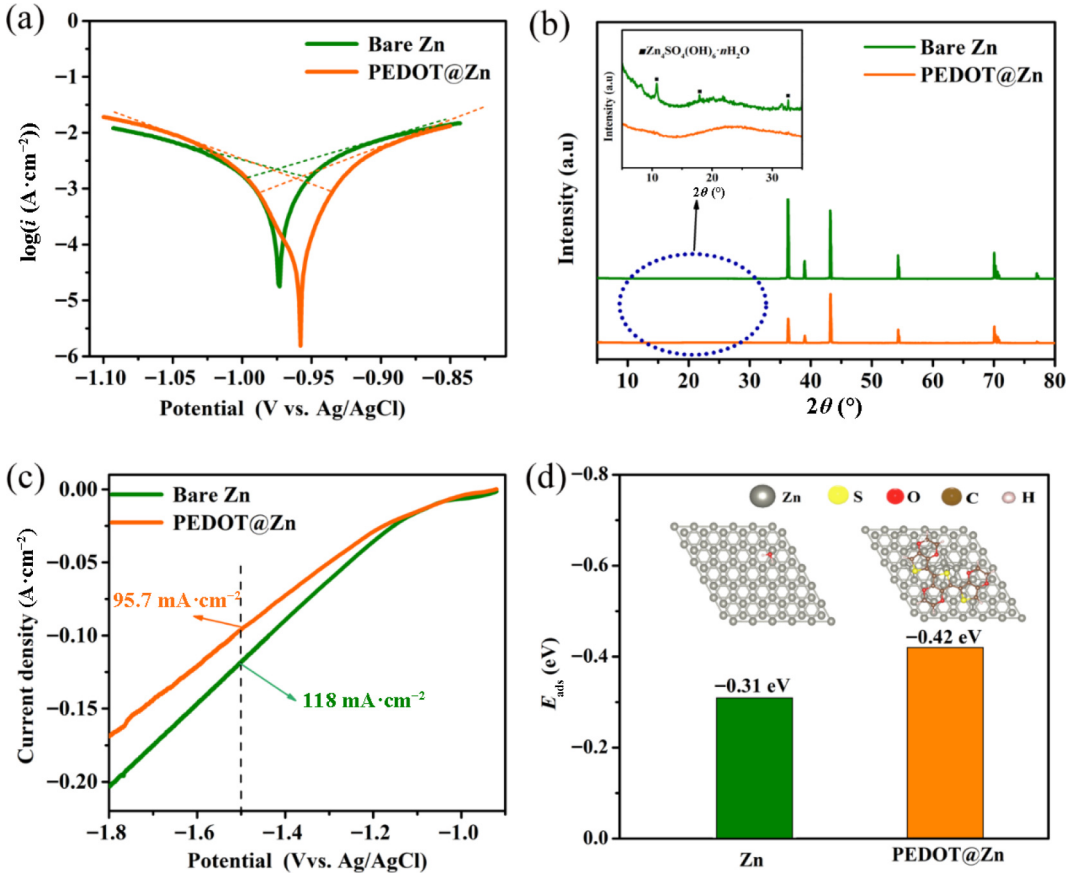

Figure 5 (a) Tafel polarization curves of bare Zn and PEDOT@Zn electrodes; (b) X-ray diffraction patterns of bare Zn and PEDOT@Zn after immersing in 2 M $ZnSO_4$ for 7 days; (c) LSV curves of bare Zn and PEDOT@Zn electrodes; (d) water adsorption energies of bare Zn and PEDOT@Zn electrodes.

concentration gradients during the cycling process [2, 56, 57]. The results of adsorption energy calculations revealed that the adsorption energy of water on PEDOT@Zn (−0.42 eV) was higher than that on pure zinc (−0.31 eV), as shown in Fig. 5(d). This indicates that the introduction of the PEDOT coating enhances water adsorption, which explains the contact angle test results. However, PEDOT@Zn has higher adsorption energy for zinc ions than water molecules, so it is preferred to adsorb zinc ions. This finding is conducive to reducing the direct adsorption of zinc to water and thus mitigating hydrogen evolution side reactions, while also accelerating the desolvation process of hydrated zinc ions, beneficial for zinc ion transport and uniform distribution [58, 59].

To visualize the deposition behavior of zinc on different zinc anodes, we performed *ex-situ* and *in situ* characterizations during cycling. Initially, bare Zn and PEDOT@Zn electrodes were assembled into a capacitor with AC cathodes and cycled 1800 times at 2 $A \cdot g^{-1}$. Afterward, the cycled SEM images were observed, as shown in Figs. 6(a)–6(d). The cycled bare Zn (Figs. 6(a) and 6(b)) and PEDOT@Zn electrodes (Figs. 6(c) and 6(d)) revealed significant differences. The surface of the cycled zinc electrode exhibited numerous disordered and large dendrites, with the bare zinc structure experiencing collapse, representing a significant change compared to the initial, unreacted zinc electrode. These structural collapses likely originated from cracks on the surface of the zinc foil. In contrast, the modified electrode displayed minimal surface collapse, maintaining a smooth structure. Although a certain amount of dendrites grew, they were significantly smaller compared to bare Zn, less likely to puncture the separator and cause battery short-circuiting.

To observe the dendrite growth process for the zinc electrode and the PEDOT@Zn electrode, cycling tests were performed at 5 $mA \cdot cm^{-2}$ and monitored via optical microscopy, as shown in Fig. 6(e). For the bare Zn electrode, a small number of dendrites were observed to grow within 30 min. Due to the "tip effect", these initially grown dendrites continued to proliferate [60]. After 120 min of cycling, numerous distinct and unevenly distributed dendrites were observed on the electrode surface, posing a significant risk of battery short-circuiting. In comparison, the modified electrode showed no significant dendrite growth within 30 min. Only after 60 min did a small number of dendrites emerge and even after 120 min, only small and uniformly distributed dendrites were present on the electrode surface, favorable for battery cycling. This is attributed to the efficient stripping and uniform deposition of zinc ions on the modified electrode.

To further elucidate the details of the nucleation and growth mechanisms, we performed chronoamperometric measurements on symmetric batteries of pure zinc and PEDOT@Zn at −150 mV, as depicted in Fig. S13 in the ESM. The continuous increase in the current density of pure zinc electrode within about 498 s indicates the disordered nucleation and growth of zinc ions [61–64], which is attributed to the 2D diffusion of zinc ions, leading to a higher likelihood of "tip effect" and dendrite growth, as illustrated in (Fig. S14 in the ESM). The current on the PEDOT@Zn electrode is smaller and stabilizes rapidly after 296 s, indicating that the abundant nucleation sites on the electrode surface inhibit the two-dimensional diffusion of Zn^{2+}. These results confirm that the

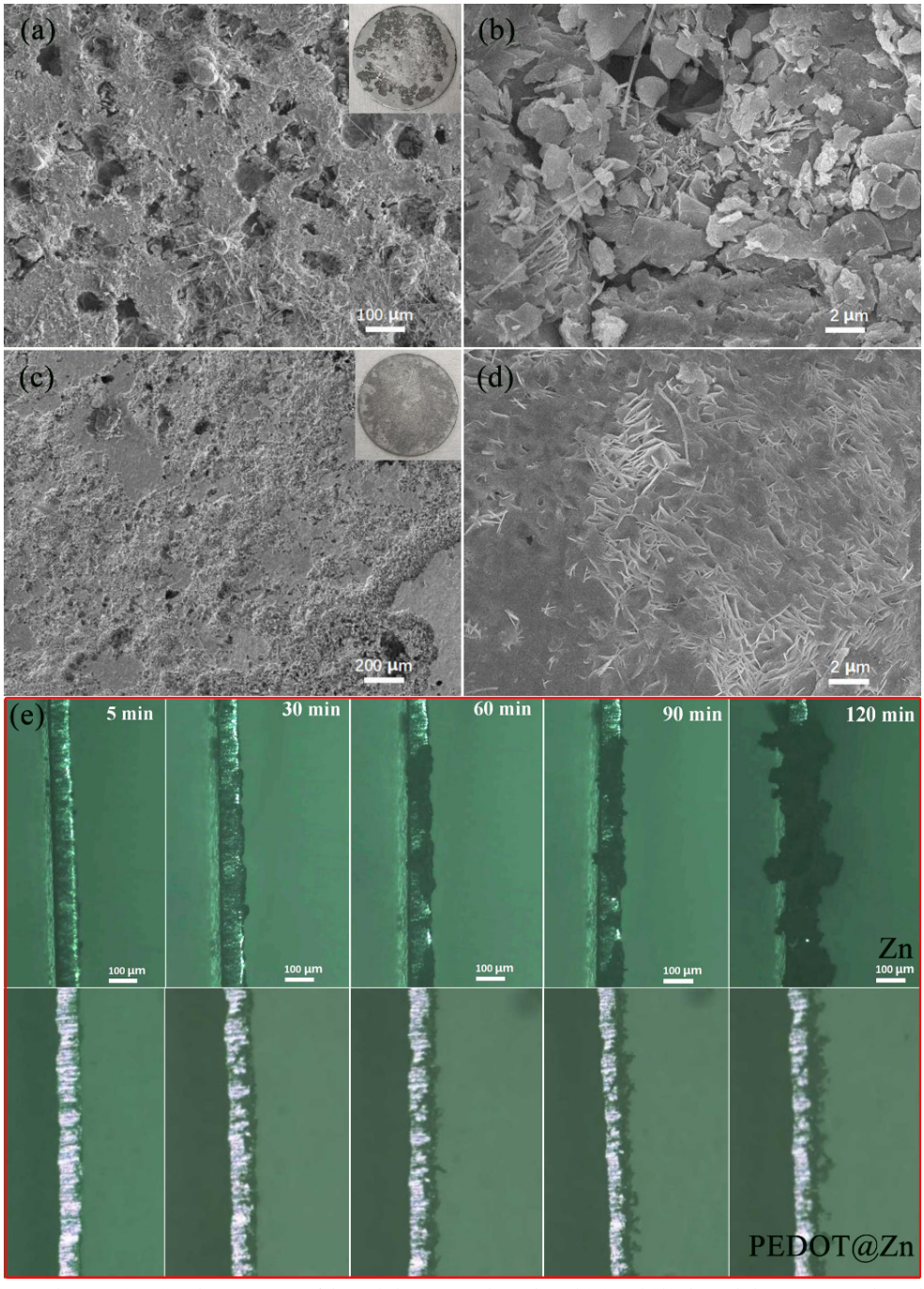

Figure 6 ((a) and (b))Optical images (inset) and SEM images of the cycled pure zinc electrode and ((c) and (d)) the cycled PEDOT@Zn electrode; (e) optical images of dendrite growth on pure zinc and PEDOT@Zn electrode at 5 mA·cm^{-2}.

introduction of a PEDOT layer on the Zn anode surface can regulate the deposition behavior of Zn^{2+}, suppressing two-dimensional diffusion and thus inhibiting dendrite formation on the Zn metal anode.

Based on the experimental data mentioned above, we propose a schematic diagram of the mechanism of the PEDOT protective layer inhibiting dendrite growth, as shown in Fig. 7(a). For pure zinc, the presence of scratches and protrusions on the surface results in a locally higher surface energy or surface area, leading to the preferential nucleation of zinc ions at these sites. As the cycling progresses, the tip effect formed by these nucleation sites drives the adsorption and reduction of more Zn^{2+} at these sites, resulting in the growth of a large number of Zn dendrites. Furthermore, water molecules can directly contact the zinc surface, causing water decomposition and side reactions. The PEDOT protective layer serves as an electrostatic shield, inhibiting dendrite growth by preventing the accumulation of ions/electrons. At the same time, the PEDOT protective layer can isolate the direct contact between zinc anode and electrolyte and can play a role in reducing side reactions and inhibiting the generation of by-products and these by-products and side reactions as well as the growth of dendrites are important reasons affecting the stability of zinc anode. Specifically, the PEDOT protective layer, with its abundant polar groups, provides sites for the adsorption or coordination of Zn ions,

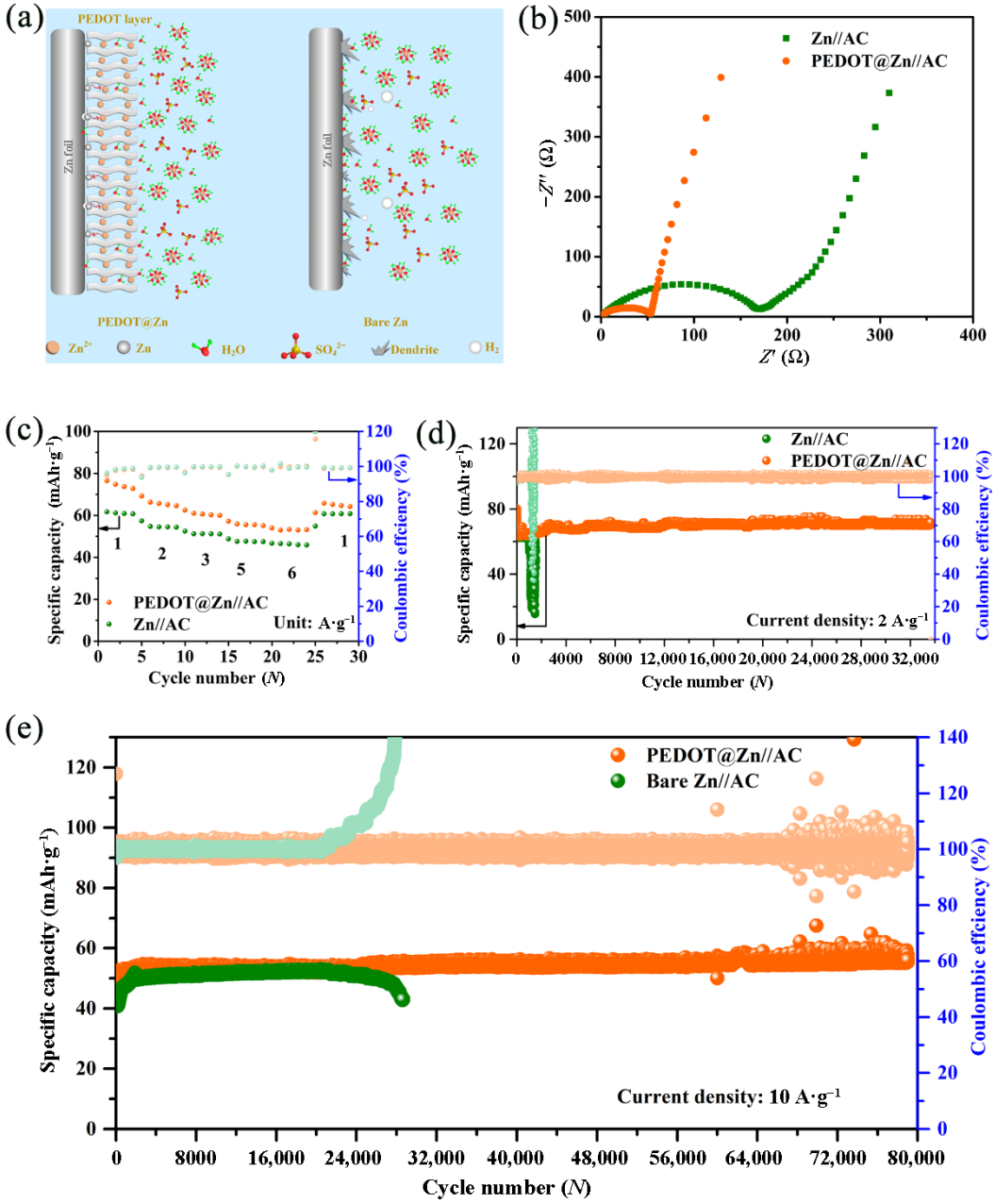

Figure 7 (a) Schematic diagram of the mechanism of PEDOT for suppressing Zn dendrite; (b) EIS tests and (c) rate performance of Zn//AC and PEDOT@Zn//AC capacitors; charge–discharge cycling of Zn//AC and PEDOT@Zn//AC capacitor at current densities of (d) 2 A·g^{-1} and (e) 10 A·g^{-1}.

facilitating the migration of Zn ions along the polymer chain to the reaction interface [65–68]. When the hydrated zinc ions diffuse to the surface of the zinc anode, the water molecules will be adsorbed by some polar groups in the PEDOT protective layer on the surface of the zinc, accelerating the desolvation process [69]. The zinc ions will also be adsorbed by the zincophilic groups of O and S in the PEDOT protective layer and the adsorption of zinc ions is stronger than that of water molecules. The zinc ions will preferentially enter the ion diffusion channel in the coatings and water molecules are adsorbed to the surface of the coating, so that the whole zinc ion of desolvation and diffusion process is completed. Because of the adsorption of water molecules by the coating, the possibility of contact between the zinc surface and zinc metal is reduced, which affects the possibility of zinc metal being corroded by hydrogen evolution. Consequently, the introduction of the PEDOT protective layer can effectively inhibit the growth of zinc dendrites and the occurrence of side reactions.

A typical PEDOT@Zn//AC capacitor was assembled to explore the feasibility of the integrated PEDOT@Zn anode. Cyclic voltammetry tests on bare Zn and PEDOT@Zn capacitors (Fig. S15 in the ESM) revealed that the modified battery exhibited a larger CV area and stronger redox peaks, indicating a greater capacity and better oxidation-reduction performance of the PEDOT@Zn//AC capacitor. EIS tests on the assembled Zn//AC and PEDOT@Zn//AC capacitors (Fig. 7(b)) showed that the PEDOT@Zn//AC capacitor exhibited a lower electron transfer impedance (69.8 Ω) compared to the Zn//AC capacitor (169.2 Ω), indicating that the PEDOT coating facilitates zinc electron transfer and effectively reduces ion transfer impedance. Rate capability tests were conducted on Zn//AC and PEDOT@Zn//AC capacitors at

different current densities (Fig. 7(c)), revealing that the specific capacity of PEDOT@Zn//AC capacitor was higher than that of Zn//AC capacitor at all current densities, due to the effective suppression of side reactions by the PEDOT coating. When the current density is 1, 2, 3, 5 and 6 $A \cdot g^{-1}$, the specific capacities of PEDOT@Zn//AC capacitor are 76.5, 66.3, 61.0, 55.9 and 53.2 $mAh \cdot g^{-1}$, respectively, which are higher than 61.7, 54.7, 51.2, 47.6 and 45.9 of Zn//AC capacitor (Fig. S16 in the ESM). The charge–discharge cycling of Zn//AC capacitors at 2 $A \cdot g^{-1}$ (Fig. 7(d)) exhibited a rapid capacity decay after only 2500 cycles, while the PEDOT@Zn//AC capacitor could maintain a capacity retention of ~ 89.5% after 34,000 cycles. While at a current density of 10 $A \cdot g^{-1}$, the PEDOT@Zn//AC capacitor retained a capacity retention of 137% after 80,000 cycles, while the Zn//AC capacitor experienced a rapid capacity decay after only 25,000 cycles (Fig. 7(e)). This demonstrates that the PEDOT protective layer significantly enhances the cycling capability of the capacitor.

4 Conclusions

In summary, a simple *in situ* electropolymerization method has been employed and a surface protective layer of hydrophilic PEDOT has been deposited on the Zn surface. The PEDOT protective layer provides corrosion resistance while also promoting the uniform diffusion of Zn^{2+} across the electrode surface. The theoretical and experimental results show that compared with pure zinc foil, the modified zinc foil has a faster kinetic process and better cyclic stability. At the same time, it helps to inhibit the growth of zinc dendrites and the side reaction. Hence, the optimized PEDOT@Zn symmetric battery exhibited a cycling stability exceeding 1250 h at 0.5 $mA \cdot cm^{-2}$ and 0.25 $mAh \cdot cm^{-2}$, with a significantly reduced overpotential (from 91.8 to 35 mV). When paired with AC as a cathode, the Zn-ion capacitors can stably cycle 80,000 times at 10 $A \cdot g^{-1}$. In this study, a simple and effective zinc metal modification technology is proposed, which is helpful to improve the cycle stability and corrosion problems of zinc-based water batteries and has a wide application prospect.

Electronic Supplementary Material: Supplementary material (further details of the cycle performance test of PEDOT@Zn of different thicknesses, XRD patterns, EIS plots of bare zinc and PEDOT@Zn symmetric batteries at different temperatures, nucleation overpotentials measurements, contact angles, chronoamperometric measurements, cyclic voltammetry tests and comparison of symmetric cells data) is available in the online version of this article at https://doi.org/10.26599/NR.2025.94907037.

Data availability

All data needed to support the conclusions in the paper are presented in the manuscript and the Electronic Supplementary Material. Additional data related to this paper may be requested from the corresponding author upon request.

Acknowledgements

We are extremely grateful to the research fund of the National Natural Science Foundation of China (Nos. 21902084, 52222203 and 52073008), the Natural Science Foundation of Hubei Province (No. 2022CFB354) and the 111 Project of Hubei Province (No. 2018-19-1) for financial support.

Declaration of competing interest

All the contributing authors report no conflict of interests in this work.

Author contribution statement

D. B. L.: Date curation, validation, writing manuscript. P. Z.: Date curation. X. W. L.: Experimental design, project administration, funding acquisition. P. P. S.: Experimental design, project administration. X. H. S.: Experimental design, project administration. H. W. Z.: Project administration, funding acquisition. All authors have approved the final manuscript.

Use of AI statement

None.

References

[1] Li, B.; Liu, S. D.; Geng, Y. F.; Mao, C. W.; Dai, L.; Wang, L.; Jun, S. C.; Lu, B. G.; He, Z. X.; Zhou, J. Achieving stable zinc metal anode via polyaniline interface regulation of Zn ion flux and desolvation. *Adv. Funct. Mater.* **2024**, *34*, 2214033.

[2] Zhang, Y. Z.; Cao, Z. J.; Liu, S. J.; Du, Z. G.; Cui, Y. L. S.; Gu, J. N.; Shi, Y. Z.; Li, B.; Yang, S. B. Charge-enriched strategy based on mxene-based polypyrrole layers toward dendrite-free zinc metal anodes. *Adv. Energy Mater.* **2022**, *12*, 2103979.

[3] He, H. B.; Qin, H. Y.; Wu, J.; Chen, X. F.; Huang, R. S.; Shen, F.; Wu, Z. R.; Chen, G. N.; Yin, S. B.; Liu, J. Engineering interfacial layers to enable Zn metal anodes for aqueous zinc-ion batteries. *Energy Storage Mater.* **2021**, *43*, 317–336.

[4] Li, X. J.; Tang, Y. C.; Lv, H. M.; Wang, W. L.; Mo, F. N.; Liang, G. J.; Zhi, C. Y.; Li, H. F. Recent advances in flexible aqueous zinc-based rechargeable batteries. *Nanoscale* **2019**, *11*, 17992–18008.

[5] Tao, F.; Liu, Y.; Ren, X. Y.; Wang, J.; Zhou, Y. Z.; Miao, Y. J.; Ren, F. Z.; Wei, S. Z.; Ma, J. M. Different surface modification methods and coating materials of zinc metal anode. *J. Energy Chem.* **2022**, *66*, 397–412.

[6] Zhao, L. L.; Zhao, S.; Zhang, N.; Wang, P. F.; Liu, Z. L.; Xie, Y.; Shu, J.; Yi, T. F. Construction of stable Zn metal anode by inorganic functional protective layer toward long-life aqueous Zn-ion battery. *Energy Storage Mater.* **2024**, *71*, 103628.

[7] Wang, T. T.; Li, C. P.; Xie, X. S.; Lu, B. G.; He, Z. X.; Liang, S. Q.; Zhou, J. Anode materials for aqueous zinc ion batteries: Mechanisms, properties, and perspectives. *ACS Nano* **2020**, *14*, 16321–16347.

[8] Wang, C. L.; Gao, Y. X.; Sun, L. S.; Zhao, Y.; Yin, D. M.; Wang, H. R.; Cao, J. C.; Cheng, Y.; Wang, L. M. Anti-catalytic and zincophilic layers integrated zinc anode towards efficient aqueous batteries for ultra-long cycling stability. *Nano Res.* **2022**, *15*, 8076–8082.

[9] Zhu, Z. H.; Jin, H. R.; Xie, K. F.; Dai, S. M.; Luo, Y. X.; Qi, B.; Wang, Z. D.; Zhuang, X. Y.; Liu, K. S.; Hu, B. et al. Molecular-level Zn-ion transfer pump specifically functioning on (002) facets enables durable Zn anodes. *Small* **2022**, *18*, 2204713.

[10] Shi, M. Y.; Zhang, J. L.; Tang, G. C.; Wang, B.; Wang, S.; Ren, X. X.; Li, G. J.; Chen, W. H.; Liu, C. T.; Shen, C. Y. Polyzwitterionic cross-linked double network hydrogel electrolyte enabling high-stable Zn anode. *Nano Res.* **2024**, *17*, 5278–5287.

[11] Li, Y. H.; Yao, H.; Liu, X. J.; Yang, X. T.; Yuan, D. Roles of electrolyte additive in Zn chemistry. *Nano Res.* **2023**, *16*, 9179–9194.

[12] Zhou, S.; Meng, X. Y.; Chen, Y. N.; Li, J. W.; Lin, S. Y.; Han, C.; Ji, X. B.; Chang, Z.; Pan, A. Q. Zinc-ion anchor induced highly reversible Zn anodes for high performance Zn-ion batteries. *Angew. Chem., Int. Ed.* **2024**, *136*, e202403050.

[13] Zheng, T.; Huang, Z. N.; Ge, H. Y.; Hu, P. F.; Fan, X. Y.; Jia, B. B. Applying machine learning to design delicate amorphous micro-nano materials for rechargeable batteries. *Energy Storage Mater.* **2024**, *71*, 103614.
[14] Zhang, B. H.; Jiang, T.; Zhou, X. Y.; Fan, X. Y.; Jia, B. B.; Li, L. D. Unlocking supercapacitive energy storage potential: Catalyzing electrochemically inactive manganese oxides to active MnO_2 via heterostructure reconstruction. *Nano Res.* **2024**, *17*, 5897–5906.
[15] Sun, B. H.; Xu, M. Y.; Li, X. X.; Zhang, B. H.; Hao, R.; Fan, X. Y.; Jia, B. B.; She, D. S. Unlocking single-atom catalysts via amorphous substrates. *Nano Res.* **2024**, *17*, 3533–3546.
[16] Lee, K.; Kim, E. J.; Kim, J.; Kim, K. H.; Lee, Y. J.; Lee, M. J.; Ryu, K.; Shin, S.; Choi, J.; Kwon, S. H. et al. Coordination engineering of N, O Co-doped cu single atom on porous carbon for high performance zinc metal anodes. *Adv. Energy Mater.* **2024**, *14*, 2303803.
[17] Qu, M.; Chen, Z.; Sun, Z. Y.; Zhou, D. N.; Xu, W. J.; Tang, H.; Gu, H. F.; Liang, T.; Hu, P. F.; Li, G. W. et al. Rational design of asymmetric atomic Ni-P_1N_3 active sites for promoting electrochemical CO_2 reduction. *Nano Res.* **2023**, *16*, 2170–2176.
[18] Yang, S. N.; Du, H. X.; Li, Y. T.; Wu, X. S.; Xiao, B. S.; He, Z. X.; Zhang, Q. B.; Wu, X. W. Advances in the structure design of substrate materials for zinc anode of aqueous zinc ion batteries. *Green Energy Environ.* **2023**, *8*, 1531–1552.
[19] Cao, Z. Y.; Zhu, X. D.; Xu, D. X.; Dong, P.; Chee, M. O. L.; Li, X. J.; Zhu, K. Y.; Ye, M. X.; Shen, J. F. Eliminating Zn dendrites by commercial cyanoacrylate adhesive for zinc ion battery. *Energy Storage Mater.* **2021**, *36*, 132–138.
[20] He, H. B.; Tong, H.; Song, X. Y.; Song, X. P.; Liu, J. Highly stable Zn metal anodes enabled by atomic layer deposited Al_2O_3 coating for aqueous zinc-ion batteries. *J. Mater. Chem. A* **2020**, *8*, 7836–7846.
[21] Xu, Y.; Zheng, X. H.; Sun, J. F.; Wang, W. P.; Wang, M. M.; Yuan, Y.; Chuai, M.; Chen, N.; Hu, H. L.; Chen, W. Nucleophilic interfacial layer enables stable Zn anodes for aqueous Zn batteries. *Nano Lett.* **2022**, *22*, 3298–3306.
[22] Kresse, G.; Hafner, J. *Ab initio* molecular dynamics for liquid metals. *Phys. Rev. B* **1993**, *47*, 558–561.
[23] Kresse, G.; Hafner, J. *Ab initio* molecular-dynamics simulation of the liquid-metal-amorphous-semiconductor transition in germanium. *Phys. Rev. B* **1994**, *49*, 14251–14269.
[24] Perdew, J. P.; Burke, K.; Ernzerhof, M. Generalized gradient approximation made simple. *Phys. Rev. Lett.* **1996**, *77*, 3865–3868.
[25] Kresse, G.; Joubert, D. From ultrasoft pseudopotentials to the projector augmented-wave method. *Phys. Rev. B* **1999**, *59*, 1758–1775.
[26] Blöchl, P. E.; Först, C. J.; Schimpl, J. Projector augmented wave method: *Ab initio* molecular dynamics with full wave functions. *Bull. Mater. Sci.* **2003**, *26*, 33–41.
[27] Poverenov, E.; Li, M.; Bitler, A.; Bendikov, M. Major effect of electropolymerization solvent on morphology and electrochromic properties of PEDOT films. *Chem. Mater.* **2010**, *22*, 4019–4025.
[28] Shi, Y. D.; Zhang, Y.; Tang, K.; Song, Y. B.; Cui, J. W.; Shu, X.; Wang, Y.; Liu, J. Q.; Wu, Y. C. *In situ* growth of PEDOT/graphene oxide nanostructures with enhanced electrochromic performance. *RSC Adv.* **2018**, *8*, 13679–13685.
[29] Stempien, Z.; Rybicki, E.; Rybicki, T.; Kozanecki, M. Reactive inkjet printing of PEDOT electroconductive layers on textile surfaces. *Synth. Met.* **2016**, *217*, 276–287.
[30] Drewelow, G.; Song, H. W.; Jiang, Z. T.; Lee, S. Factors controlling conductivity of PEDOT deposited using oxidative chemical vapor deposition. *Appl. Surf. Sci.* **2020**, *501*, 144105.
[31] Zhao, W.; Perera, I. P.; Khanna, H. S.; Dang, Y. L.; Li, M. X.; Posada, L. F.; Tan, H. Y.; Suib, S. L. Modification of zinc anodes by *in situ* ZnO coating for high-performance aqueous zinc-ion batteries. *ACS Appl. Energy Mater.* **2024**, *7*, 1172–1181.
[32] Kang, L. T.; Cui, M. W.; Jiang, F. Y.; Gao, Y. F.; Luo, H. J.; Liu, J. J.; Liang, W.; Zhi, C. Y. Nanoporous $CaCO_3$ coatings enabled uniform Zn stripping/plating for long-life zinc rechargeable aqueous batteries. *Adv. Energy Mater.* **2018**, *8*, 1801090.
[33] Sui, B. B.; Sha, L.; Wang, P. F.; Gong, Z.; Zhang, Y. H.; Wu, Y. H.; Zhao, L. N.; Tang, J. J.; Shi, F. N. Salt solution etching to construct micro-gullies on the surface of Zn anodes enhances anodes performance in aqueous zinc-ion batteries. *J. Colloid Interface Sci.* **2024**, *653*, 159–169.
[34] Sha, L.; Sui, B. B.; Wang, P. F.; Gong, Z.; Zhang, Y. H.; Wu, Y. H.; Zhao, L. N.; Shi, F. N. Printing 3D mesh-like grooves on zinc surface to enhance the stability of aqueous zinc ion batteries. *J. Colloid Interface Sci.* **2023**, *647*, 421–428.
[35] Zhou, J. H.; Wu, F.; Mei, Y.; Hao, Y. T.; Li, L.; Xie, M.; Chen, R. J. Establishing thermal infusion method for stable zinc metal anodes in aqueous zinc-ion batteries. *Adv. Mater.* **2022**, *34*, 2200782.
[36] Zhang, X. T.; Li, J. X.; Liu, D. Y.; Liu, M. K.; Zhou, T. S.; Qi, K. W.; Shi, L.; Zhu, Y. C.; Qian, Y. T. Ultra-long-life and highly reversible Zn metal anodes enabled by a desolvation and deanionization interface layer. *Energy Environ. Sci.* **2021**, *14*, 3120–3129.
[37] Kim, J. Y.; Liu, G. C.; Shim, G. Y.; Kim, H.; Lee, J. K. Functionalized Zn@ZnO hexagonal pyramid array for dendrite-free and ultrastable zinc metal anodes. *Adv. Funct. Mater.* **2020**, *30*, 2004210.
[38] Zhang, N. N.; Huang, S.; Yuan, Z. S.; Zhu, J. C.; Zhao, Z. F.; Niu, Z. Q. Direct self-assembly of MXene on Zn anodes for dendrite-free aqueous zinc-ion batteries. *Angew. Chem., Int. Ed.* **2021**, *60*, 2861–2865.
[39] Xie, X. S.; Liang, S. Q.; Gao, J. W.; Guo, S.; Guo, J. B.; Wang, C.; Xu, G. Y.; Wu, X. W.; Chen, G.; Zhou, J. Manipulating the ion-transfer kinetics and interface stability for high-performance zinc metal anodes. *Energy Environ. Sci.* **2020**, *13*, 503–510.
[40] Gou, Q. Z.; Chen, Z. Y.; Luo, H. R.; Deng, J. B.; Zhang, B.; Xu, N.; Cui, J. Y.; Zheng, Y. J.; Li, M.; Li, J. Synergistic modulation of mass transfer and parasitic reactions of Zn metal anode via bioinspired artificial protection layer. *Small* **2024**, *20*, 2305902.
[41] Chen, X. H.; Shi, X. D.; Ruan, P. C.; Tang, Y.; Sun, Y. Y.; Wong, W. Y.; Lu, B. G.; Zhou, J. Construction of an artificial interfacial layer with porous structure toward stable zinc-metal anodes. *Small Sci.* **2023**, *3*, 2300007.
[42] Huyan, X. D.; Yi, Z. H.; Sang, Z. Y.; Tan, S. D.; Liu, J. X.; Chen, R.; Si, W. P.; Liang, J.; Hou, F. Polyethylene glycol coating on zinc powder surface: Applications in dendrite-free zinc anodes with enhanced utilization rate. *Appl. Surf. Sci.* **2023**, *614*, 156209.
[43] Wu, Y.; Zhang, T.; Chen, L. N.; Zhu, Z. H.; Cheng, L. K.; Gu, S.; Li, Z. Q.; Tong, Z. Q.; Li, H.; Li, Y. F. et al. Polymer chain-guided ion transport in aqueous electrolytes of Zn-ion batteries. *Adv. Energy Mater.* **2023**, *13*, 2300719.
[44] Qin, Y.; Wang, X. Preventing dissolution of cathode active materials by ion-anchoring zeolite-based separators for durable aqueous zinc batteries. *Angew. Chem., Int. Ed.* **2024**, *63*, e202315464.
[45] Liu, S. Y.; Li, S. J.; Li, Y. Research progress on energy storage and anode protection of aqueous zinc-ion battery. *ChemElectroChem* **2024**, *11*, e202400188.
[46] Wang, S. J.; Yang, Z.; Chen, B. T.; Zhou, H.; Wan, S. F.; Hu, L. Z.; Qiu, M.; Qie, L.; Yu, Y. A highly reversible, dendrite-free zinc metal anodes enabled by a dual-layered interface. *Energy Storage Mater.* **2022**, *47*, 491–499.
[47] Hao, J. N.; Li, B.; Li, X. L.; Zeng, X. H.; Zhang, S. L.; Yang, F. H.; Liu, S. L.; Li, D.; Wu, C.; Guo, Z. P. An in-depth study of Zn metal surface chemistry for advanced aqueous Zn-ion batteries. *Adv. Mater.* **2020**, *32*, 2003021.
[48] Li, J. B.; Zhang, S. M.; Wu, Y.; Jin, B. W.; Shao, M. F. The ultrathin prenucleation interface-stabilized metal Zn anode toward high-performance flexible Zn-batteries. *Mater. Today Energy* **2021**, *22*, 100849.
[49] Han, J.; Euchner, H.; Kuenzel, M.; Hosseini, S. M.; Groß, A.; Varzi, A.; Passerini, S. A thin and uniform fluoride-based artificial

interphase for the zinc metal anode enabling reversible Zn/MnO_2 batteries. *ACS Energy Lett.* **2021**, *6*, 3063–3071.
[50] Cai, Z.; Wang, J. D.; Sun, Y. M. Anode corrosion in aqueous Zn metal batteries. *eScience* **2023**, *3*, 100093.
[51] Bayaguud, A.; Fu, Y. P.; Zhu, C. B. Interfacial parasitic reactions of zinc anodes in zinc ion batteries: Underestimated corrosion and hydrogen evolution reactions and their suppression strategies. *J. Energy Chem.* **2022**, *64*, 246–262.
[52] Chen, M.; Guo, X. J.; Jiang, X.; Farhadi, B.; Guo, X.; Zhu, Y.; Zhang, H. X.; Liu, S. Z. Multi-group polymer coating on Zn anode for high overall conversion efficiency photorechargeable zinc-ion batteries. *Angew. Chem., Int. Ed.* **2024**, *63*, e202410011
[53] Zhao, N. N.; Zhang, Y. T.; Zhang, Z. K.; Han, C.; Liang, Y. Y.; Li, J. T.; Wang, X. L.; Dai, L.; Wang, L.; He, Z. X. Polyaniline functionalized separator as synergistic medium for aqueous zinc-ion batteries. *J. Colloid Interface Sci.* **2023**, *642*, 421–429.
[54] Lv, D.; Peng, H. L.; Wang, C.; Liu, H. X.; Wang, D. D.; Yang, J.; Qian, Y. T. Rational screening of metal coating on Zn anode for ultrahigh-cumulative-capacity aqueous zinc metal batteries. *J. Energy Chem.* **2023**, *84*, 81–88.
[55] Shen, Y. F.; Liu, Y.; Sun, K. S.; Gu, T. T.; Wang, G.; Yang, Y.; Pang, J. X.; Zheng, Y.; Yang, X. D.; Chen, L. Zincophilic $Ti_3C_2Cl_2$ MXene and anti-corrosive Cu NPs for synergistically regulated deposition of dendrite-free Zn metal anode. *J. Mater. Sci. Technol.* **2024**, *169*, 137–147.
[56] Wang, Y. J.; Sun, H. Y.; Li, N.; Chen, K. Y.; Yang, X. B.; Liu, H. Y.; Zheng, G. M.; Liu, J.; Wu, Z. J.; Zhai, L. P. et al. Highly reversible and stable zinc anode enabled by a fully conjugated porous organic polymer protective layer. *ACS Appl. Energy Mater.* **2022**, *5*, 2375–2383.
[57] Zeng, Y. X.; Zhang, X. Y.; Qin, R. F.; Liu, X. Q.; Fang, P. P.; Zheng, D. Z.; Tong, Y. X.; Lu, X. H. Dendrite-free zinc deposition induced by multifunctional CNT frameworks for stable flexible Zn-ion batteries. *Adv. Mater.* **2019**, *31*, 1903675.
[58] Yang, J. Z.; Wang, S.; Du, L. Y.; Bi, S. S.; Zhu, J. C.; Liu, L. L.; Niu, Z. Q. Thermal-cyclized polyacrylonitrile artificial protective layers toward stable zinc anodes for aqueous zinc-based batteries. *Adv. Funct. Mater.* **2024**, *34*, 2314426.
[59] Zhao, S. Y.; Liu, X. T.; Chang, T.; Tang, H. Q.; Tian, T.; Weng, Q.; Liu, T. Achieving stable Zn anodes by reducing desolvation barrier and guiding homogeneous nucleation through zincophilic polymer layer. *Energy Storage Mater.* **2024**, *72*, 103769.
[60] Zhang, F.; Qian, J. W.; Dong, W. X.; Qu, Y. F.; Chen, J. W.; Wang, H.; Chen, L. F. A facile tip shielding strategy for highly reversible Zn anode. *Chem. Eng. J.* **2023**, *478*, 147406.
[61] Zhao, Z. M.; Zhao, J. W.; Hu, Z. L.; Li, J. D.; Li, J. J.; Zhang, Y. J.; Wang, C.; Cui, G. L. Long-life and deeply rechargeable aqueous Zn anodes enabled by a multifunctional brightener-inspired interphase. *Energy Environ. Sci.* **2019**, *12*, 1938–1949.
[62] Li, L.; Yang, H.; Yuan, Z. Y.; Tan, Y. C.; Zhang, Y. M.; Miao, C. L.; Chen, D.; Li, G. S.; Han, W. The organic ligand etching method for constructing *in situ* terraced protective layer toward stable aqueous Zn anode. *Small* **2023**, *19*, 2305554.
[63] Shen, Y. F.; Fu, P. J.; Liu, J. J.; Sun, K. S.; Wen, H. Z.; Liu, P.; Lv, H.; Gu, T. T.; Yang, X. D.; Chen, L. Highly stable Zn anodes realized by 3D zincophilic and hydrophobic interphase buffer layer. *Nano Res. Energy* **2024**, *3*, e9120115.
[64] Wu, M. M.; Wang, X. C.; Zhang, F.; Xiang, Q.; Li, Y.; Guo, J. X. Highly reversible and stable Zn metal anodes realized using a trifluoroacetamide electrolyte additive. *Energy Environ. Sci.* **2024**, *17*, 619–629.
[65] Hao, J. N.; Li, X. L.; Zhang, S. L.; Yang, F. H.; Zeng, X. H.; Zhang, S.; Bo, G. Y.; Wang, C. S.; Guo, Z. P. Designing dendrite-free zinc anodes for advanced aqueous zinc batteries. *Adv. Funct. Mater.* **2020**, *30*, 2001263.
[66] Chen, P.; Yuan, X. H.; Xia, Y. B.; Zhang, Y.; Fu, L. J.; Liu, L. L.; Yu, N. F.; Huang, Q. H.; Wang, B.; Hu, X. W. et al. An artificial polyacrylonitrile coating layer confining zinc dendrite growth for highly reversible aqueous zinc-based batteries. *Adv. Sci.* **2021**, *8*, 2100309.
[67] Shin, J.; Lee, J.; Kim, Y.; Park, Y.; Kim, M.; Choi, J. W. Highly reversible, grain-directed zinc deposition in aqueous zinc ion batteries. *Adv. Energy Mater.* **2021**, *11*, 2100676.
[68] Nie, W.; Cheng, H. W.; Sun, Q. C.; Liang, S. Q.; Lu, X. G.; Lu, B. G.; Zhou, J. Design strategies toward high-performance Zn metal anode. *Small Methods* **2024**, *8*, 2201572.
[69] Zhao, N. N.; Liang, Y. Y.; Huo, W. J.; Zhu, X. Y.; He, Z. X.; Zhang, Z. K.; Zhang, Y. T.; Wu, X. W.; Dai, L.; Zhu, J. et al. Separator functionalization enables high-performance zinc anode via ion-migration regulation and interfacial engineering. *Chinese Chemical Letters* **2024**, *35*, 109332.

This is an open access article under the terms of the Creative Commons Attribution 4.0 International License (CC BY 4.0, https://creativecommons.org/licenses/by/4.0/).

© The Author(s) 2025. Published by Tsinghua University Press.